Numerical modeling of near-surface seismic scattering by the partitioned domain method

Ivan J. Sánchez-Galvis *, William Agudelo†, Daniel O. Trad‡, and Daniel Sierra*,

ABSTRACT

Accurate modeling of near-surface seismic scattering (NSS) is crucial for reducing noise and enhancing the quality and interpretability of seismic data. This process enables the identification of specific characteristics of NSS , leading to the development of more effective techniques to attenuate it. While various methods having been developed to model NSS from elastic wave forward modeling, they often present constraints in considering complex overburdens with substantial topographic variations or random heterogeneous media. In this work, we present the partitioned domian method (PDM) to address these limitations. The method involves two stages of elastic wave modeling to generate synthetic seismic data with and without NSS. The first stage uses the entire earth model to generate the total wavefield (TW), encompassing all seismic wave types. The second stage employs the near-surface portion of the earth model to yield the near-surface wavefield (NW), inclusive of direct waves, Rayleigh waves, and NSS. A deep wavefield (DW), comprising body wave reflections and refractions from deeper structures, is then derived by subtracting the NW from the TW. To study the performance of the proposed method, we conduct a numerical example using the SEAM Foothills Phase II model. The results demonstrate that our method can effectively model the NSS, enhancing the understanding of land seismic noise that facilitates the development of new attenuation techniques.

INTRODUCTION

The near-surface is the space immediately below the free-surface of the earth. This space is approximately 300 meters of deep within the scale of exploration seismology and is composed of a soil column and low-velocity, unconsolidated, heterogeneous, and weathered layers of rock Yilmaz (2015). These characteristics makes the acquired seismic data in complex land areas have near-surface scattering (NSS) that mask the desired body-waves reflections. This unwanted energy represents the most challenging noise in land seismic data processing as conventional processing techniques, like $f - k$ filters, struggle to effectively characterize and eliminate it. Therefore, modeling NSS has emerged as a crucial step in understanding how seismic waves propagate and scatter upon encountering near-surface heterogeneities. This task is typically accomplished by modeling elastic wave scattering.

Several methods for modeling elastic wave scattering have been proposed, broadly falling into two categories: analytical and numerical approaches. The analytical approach often relies on the first Born approximation for calculating single scattering. Within this approach, perturbation methods have been extensively studied and applied in numerous investigations (Hudson, 1967; Wu and Aki, 1985; Wu, 1989; Beylkin and Burridge, 1990;

*Universidad Industrial de Santander
†Centro de Innovación y Tecnología - ECOPETROL S.A.
‡CREWES - University of Calgary

Maeda et al., 2008; Sato et al., 2012). Additionally, the asymptotic method is another technique within the analytical approach, evidenced by the works of Snieder (1986) and Blonk and Herman (1994). While these methods have enhanced our understanding of scattering behavior, they exhibit limitations, especially when addressing large and high-contrast heterogeneities that violate the first Born (single-scattering) approximation.

In contrast, numerical approaches are capable of solving the full wave equation, offering an advantage when dealing with more complex background media, significant contrasts in medium parameters, and irregular interfaces. Moreover, they can generate synthetic seismograms with high accuracy over a wide range of wavelength ratios. Within this approach, the finite-difference method proposed by Robertsson and Chapman (2000) provides an efficient way to model scattering. However, it does not account for the interaction of the scattered wavefield with the free surface and bedrock layers. An alternate numerical method, the integral equation method with elastic wave numerical modeling using the moments method (Riyanti and Herman, 2005; Campman and Dwi Riyanti, 2007), not only models multiple scattering but can also handle strong contrast and large heterogeneities. Despite these strengths, the method's applicability is constrained to laterally homogeneous embedding consisting of horizontal layers, a situation often absent in areas with complex overburden. More recently, Almuhaidib and Toksöz (2014) proposed a flexible approach to modeling scattering using Finite Difference Method (FDM) with perturbation theory. This approach decomposes the medium parameters into background and perturbation parts, enabling the modeling of scattering from arbitrarily shaped scatterers and the interaction of the multiply scattered wavefield with the free surface. However, this approach assumes constant background medium parameters and employs the homogeneous wave equation for simulating the incident wavefield.

Considering the limitations of existing methodologies in modeling Near Surface Scattering (NSS) in complex overburden scenarios, we propose a novel approach called the Partitioned Domain Method (PDM) as a promising solution. The PDM addresses these challenges by partitioning the computational domain and simulating the near-surface and deep wavefields separately. In this work, we introduce the PDM and assess its effectiveness through a numerical example utilizing the SEAM foothill model. The results substantiate the PDM's capability to generate deep wavefields devoid of significant NSS energy. This innovative approach not only provides valuable insights into wavefield characteristics but also contributes to the advancement of seismic processing techniques for scattering noise attenuation.

ELASTIC WAVE MODELING IN HETEROGENEOUS MEDIA

The elastic wave equation for heterogeneous media, using operator notation, cen be written as follows:

$$L_{ij}(\rho, \lambda, \mu; t) u_j(\mathbf{x}, t) = 0 \tag{1}$$

where

$$L_{ij}(\rho,\lambda,\mu,t) = \delta_{ij}\rho(\mathbf{x})\partial_t^2 - \partial_i[\lambda(\mathbf{x})\partial_j] - \partial_j[\mu(\mathbf{x})\partial_i] - \delta_{ij}\partial_k[\mu(\mathbf{x})\partial_k]. \tag{2}$$

To analyze the scattering of elastic waves, we assume that the medium parameters deviate from the background homogeneous structure in the following manner Maeda et al. (2008); Sato et al. (2012):

$$\lambda(\mathbf{x}) = \lambda_0 + \delta\lambda(\mathbf{x}), \qquad \mu(\mathbf{x}) = \mu_0 + \delta\mu(\mathbf{x}), \qquad \rho(\mathbf{x}) = \rho_0 + \delta\rho(\mathbf{x}) \qquad \text{for } \mathbf{x} \in \mathcal{V} \tag{3}$$

where subscript zero denotes a homogeneous background medium, and $\delta\rho$, $\delta\lambda$ and $\delta\mu$ denote the fluctuation of density and Lamé coefficients in the volume region $\mathcal{V}$.

In the subsequent sections, we will study the solutions for the elastic wave equation in both homogeneous and heterogeneous media.

Homogeneous background model

In the homogeneous background model, the elastic wave equation can be represented as:

$$L_{ij}(\rho_0,\lambda_0,\mu_0;t)u_j^0(\mathbf{x},t) = 0. \tag{4}$$

Here, u^0 indicates the particle displacement that satisfies the homogeneous equation. Frequently, this equation is solved using Green's functions analysis, aiming to solve the equation for an impulsive source as follows:

$$L_{ij}(\rho_0,\lambda_0,\mu_0;\omega)G_{jk}(\mathbf{x},t) = \delta_{ik}\delta(\mathbf{x}-\mathbf{x}'), \tag{5}$$

where G_{jk} is the Green's function for displacement of the j component induced by an excitation source in the k direction. $\delta()$ represents the Dirac delta function, and $\mathbf{x}'$ designates the source coordinate location.

As deduced by Sato et al. (2012), the Green's function can be expressed as combination of several Green's functions:

$$G_{jk}(\mathbf{x},t) = \underbrace{G_{jk}^{P}(\mathbf{x},t) + G_{jk}^{Sv}(\mathbf{x},t) + G_{jk}^{Sh}(\mathbf{x},t)}_{\text{Green's functions for body waves}} + G_{jk}^{R}(\mathbf{x},t) + G_{jk}^{N}(\mathbf{x},t). \tag{6}$$

Each term on the right-hand side of this equation represents a specific wave type. The first three terms $\left(G_{jk}^{P}, G_{jk}^{Sv}, G_{jk}^{Sh}\right)$ denote the Green's function for $P-$, Sv, and $Sh-$ body

waves, respectively. The fourth term, G^R_{jk}, represents the Green's function for Rayleigh waves, while G^N_{jk} reflects the near-field effects.

By ignoring the near-field effects and combining all the body wave terms into a single term (G^B_{jk}), the total Green's function can be simplified as:

$$G_{jk}(\mathbf{x},t) = G^B_{jk}(\mathbf{x},t) + G^R_{jk}(\mathbf{x},t) \tag{7}$$

This resultant total Green's function can then be utilized to generate the total background wavefield as the sum of a body wavefield and a Rayleigh wavefield as follows:

$$\mathbf{u}^0(\mathbf{x},t) = \mathbf{u}^{0,B}(\mathbf{x},t) + \mathbf{u}^{0,R}(\mathbf{x},t) \tag{8}$$

Heterogeneous model

The solution to the wave equation for a heterogeneous model can be expressed in terms of the solution for a homogeneous medium. By incorporating Eq. (3) into Eq. (2), the operator L_{ij} can be split into two terms as follows:

$$[L_{ij}(\rho_0,\lambda_0,\mu_0;t) + L_{ij}(\delta\rho,\delta\lambda,\delta\mu;t)]u_j(\mathbf{x},t) = 0. \tag{9}$$

Here, the first term on the left-hand side corresponds to the operator for the homogeneous equation, while the second term depends only on the perturbed medium parameters.

After moving the second term to the right-hand side, we obtain:

$$L_{ij}(\rho_0,\lambda_0,\mu_0;t)u_j(\mathbf{x},t) = -L_{ij}(\delta\rho,\delta\lambda,\delta\mu;t)u_j(\mathbf{x},t). \tag{10}$$

This equation shows that the term depending only on the perturbed medium parameters can be treated as a source term injected into the homogeneous elastic wave equation.

Consequently, the total wavefield can be expressed as the sum of an incident wavefield and a scattering wavefield as follows:

$$u_i(\mathbf{x},t) = u^0_i(\mathbf{x},t) + \int_{-\infty}^{\infty} dt' \iiint_{-\infty}^{\infty} d(\mathbf{x}')G_{ik}(\mathbf{x}-\mathbf{x}',t-t')[-L_{kj}(\delta\rho,\delta\lambda,\delta\mu;t)]u_j(\mathbf{x}',t'). \tag{11}$$

Alternatively, equation (11) can be expressed in the vector notation, such that $\mathbf{m} = (\lambda,\mu,\rho)$ and omitting the differential terms:

$$\mathbf{u} = \underbrace{\mathbf{u}^0}_{\text{incident wavefield}} + \underbrace{\int \mathbf{G}[-\mathbf{L}(\delta\mathbf{m})]\mathbf{u}}_{\text{scattering wavefield}}, \tag{12}$$

where

$$\mathbf{G} = \begin{bmatrix} G_{xx} & G_{xy} & G_{xz} \\ G_{yx} & G_{yy} & G_{yz} \\ G_{zx} & G_{zy} & G_{zz} \end{bmatrix}, \quad \mathbf{L} = \begin{bmatrix} L_{xx} & L_{xy} & L_{xz} \\ L_{yx} & L_{yy} & L_{yz} \\ L_{zx} & L_{zy} & L_{zz} \end{bmatrix}, \quad \text{and } \mathbf{u} = \begin{bmatrix} u_x \\ u_y \\ u_z \end{bmatrix}. \tag{13}$$

Notice that the scattering term in Eq. (12) depends on the total wavefield. By recursively replacing this equation within itself, we can form an infinite series, which schematically looks like:

$$\mathbf{u} = \mathbf{u}^0 + \underbrace{\int \mathbf{G}[-\mathbf{L}(\delta\mathbf{m})]\mathbf{u}^0}_{\text{first-order scattering}} + \underbrace{\int \mathbf{G}[-\mathbf{L}(\delta\mathbf{m})] \int \mathbf{G}[-\mathbf{L}(\delta\mathbf{m})]\mathbf{u}^0}_{\text{second-order scattering}} + \underbrace{\ldots}_{\text{higher-order scattering}} \tag{14}$$

This equation, known as the scattering series, demonstrates that scattering is a multiplicative process, which complicates its separation. Unlike additive noise, which can often be estimated and subtracted, multiplicative noise interacts nonlinearly with the seismic signal, making it more difficult to isolate.

The total wavefield can then be expressed as an infinite sum of scattering wavefield terms of different orders:

$$\mathbf{u} = \sum_{n=0}^{\infty} \mathbf{u}^n, \tag{15}$$

where each term $\mathbf{u}^n$ corresponds to the n-th-order scattering wavefield, which is defined as:

$$\mathbf{u}^n = \left(\int \mathbf{G}[-\mathbf{L}(\delta\mathbf{m})] \right)^n \mathbf{u}^0 \tag{16}$$

By incorporating Eq. (15) into Eq. (12), and after some manipulation, the total wavefield can be expressed as:

$$\mathbf{u} = \mathbf{u}^0 + \int \mathbf{G}[-\mathbf{L}(\delta\mathbf{m})] \left(\sum_{n=0}^{\infty} \mathbf{u}^n \right) \tag{17}$$

Finally, the total wavefield $\mathbf{u}$ can be expressed as the sum of a body wavefield $\mathbf{u}^B$ and a Rayleigh wavefield $\mathbf{u}^R$:

$$\mathbf{u} = \mathbf{u}^B + \mathbf{u}^R, \tag{18}$$

where

$$\mathbf{u}^B = \underbrace{\mathbf{u}^{0,B}}_{\text{incident body waves}} + \underbrace{\int \mathbf{G}^B[-\mathbf{L}(\delta\mathbf{m})] \left(\sum_{n=0}^{\infty} \mathbf{u}^n \right)}_{\text{body-waves scattering}}, \tag{19}$$

and

$$\mathbf{u}^R = \underbrace{\mathbf{u}^{0,R}}_{\text{incident Rayleigh waves}} + \underbrace{\int \mathbf{G}^R[-\mathbf{L}(\delta\mathbf{m})] \left(\sum_{n=0}^{\infty} \mathbf{u}^n \right)}_{\text{Rayleigh-wave scattering}}. \tag{20}$$

Note that Eq. (19) indicates that the body wavefield is expressed as the combination of incident body waves and body-wave scattering. This body-wave scattering corresponds to the multiple scattering where the last interaction results in a body wave, either P- or S-wave. Similarly, Eq. (20) shows that the Rayleigh wavefield is expressed as the combination of the incident Rayleigh wave and Rayleigh-wave scattering, which corresponds to the multiple scattering where the last interaction results in a Rayleigh wave.

First Born approximation

In the specific instance of heterogeneities exhibiting small fractional fluctuations (volume heterogeneities localized in the near-surface), the amplitude of the scattered wave is less than the incident wave. In this scenario, the scattering wavefield is approximated as single-scattering, as opposed to multiple scattering. This implies that only the first term of scattering is considered, and the total wavefield can be expressed as:

$$\mathbf{u} = \mathbf{u}^0 + \mathbf{u}^1 = \mathbf{u}^0 + \int \mathbf{G}[-\mathbf{L}(\delta\mathbf{m})]\mathbf{u}^0 \tag{21}$$

This approximation holds valid when $|\mathbf{u}^1| \ll |\mathbf{u}^0|$.

Consequently, the body wavefield and the Rayleigh wavefield are also represented as the sum of an incident wavefield and the single-scattering terms as follows:

$$\mathbf{u}^B = \mathbf{u}^{0,B} + \underbrace{\int \mathbf{G}^B[-\mathbf{L}(\delta\mathbf{m})]\mathbf{u}^{0,B}}_{\text{body-to-body waves}} + \underbrace{\int \mathbf{G}^B[-\mathbf{L}(\delta\mathbf{m})]\mathbf{u}^{0,R}}_{\text{Rayleigh-to-body waves}}, \tag{22}$$

$$\mathbf{u}^R = \mathbf{u}^{0,R} + \underbrace{\int \mathbf{G}^R[-\mathbf{L}(\delta\mathbf{m})]\mathbf{u}^{0,R}}_{\text{Rayleigh-to-Rayleigh waves}} + \underbrace{\int \mathbf{G}^R[-\mathbf{L}(\delta\mathbf{m})]\mathbf{u}^{0,B}}_{\text{body-to-Rayleigh waves}}. \tag{23}$$

Equations (22) and (23) reveal that the scattering wavefield comprises conversions between body and Rayleigh waves. The body-wave scattering consists of body-to-body and Rayleigh-to-body wave conversions. Conversely, Rayleigh-wave scattering includes Rayleigh-to-Rayleigh and body-to-Rayleigh wave conversions. Figure 1 provides a schematic representation of how seismic waves are scattered in the presence of a volume heterogeneity. There are four types of single-scattering: body-to-body, body-to-Rayleigh, Rayleigh-to-body, and Rayleigh-to-Rayleigh.

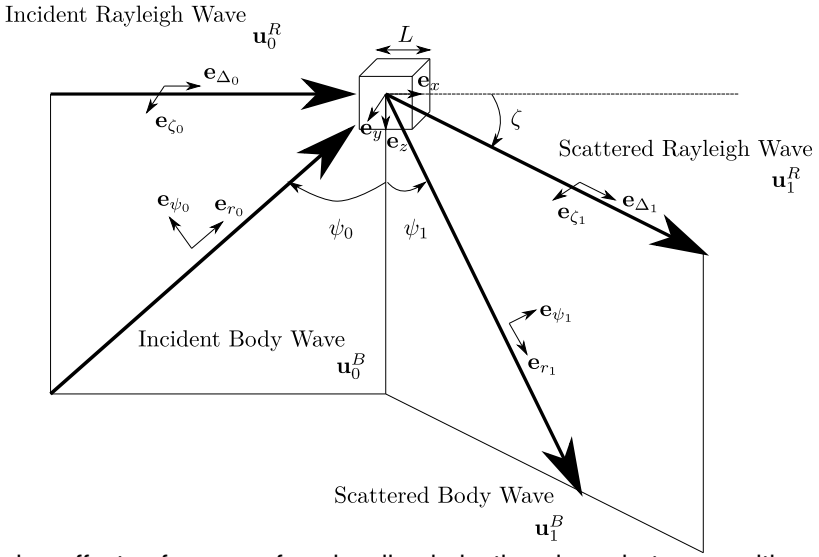

FIG. 1. Scattering effects of near-surface localized elastic volume heterogeneities. Upon the incidence of body and Rayleigh waves on the heterogeneity, both wavefields are scattered, resulting in scattered body waves and scattered Rayleigh waves.

THE PERTURBATION METHOD WITH FDM

In scenarios involving complex overburdens, the first Born approximation is not applicable due to the significant fractional fluctuations in medium parameters, leading to high amplitude scattering. Nonetheless, employing the perturbation method with FDM provides a straightforward and efficient approach to model multiple scattering without the need for the first Born approximation. This method, developed by Almuhaidib and Toksöz (2014), simulates the scattering wavefield using the following three-step process:

1) A total wavefield $\mathbf{u}$ is numerically computed using FDM with the elastic wave equation for heterogeneous media (1). This total wavefield comprises the incident $\mathbf{u}^0$ and scattering wavefield $\mathbf{u}^{sc}$ ($\mathbf{u} = \mathbf{u}^0 + \mathbf{u}^{sc}$).

2) The incident wavefield $\mathbf{u}^0$ is numerically computed with FDM using the elastic wave equation for homogeneous media (4).

3) The scattering wavefield $\mathbf{u}^{sc}$ is then obtained by subtracting the incident wavefield from the total wavefield ($\mathbf{u}^{sc} = \mathbf{u} - \mathbf{u}^0$).

To illustrate the application of this method, consider the velocity and density model depicted in Figure 2, consisting of three homogeneous layers with two heterogeneities within the first layer. The elastic wave propagation is modeled numerically by employing a 30 Hz Ricker source positioned at a depth of 10 m and a horizontal distance of 1000 m. Receivers are positioned on the surface between 250 m and 1750 m horizontal distance, with an interval spacing of 2 m. The synthetic shot gathers of the incident, total, and scattered waves are shown in Figure 3. Here, it is possible to observe the four types of single-scattering (body-to-body, body-to-Rayleigh, Rayleigh-to-body, and Rayleigh-to-Rayleigh)

Experiments conducted by Almuhaidib and Toksöz (2014) demonstrated the efficacy of this method in simulating near-surface scattering, not only under localized volume heterogeneities but also irregular bedrock interfaces. However, this method is predicated on a homogeneous background medium with constant parameters in the near-surface region. Consequently, it may not be able to handle more complex near-surface scenarios, such as those including rough topography and random media.

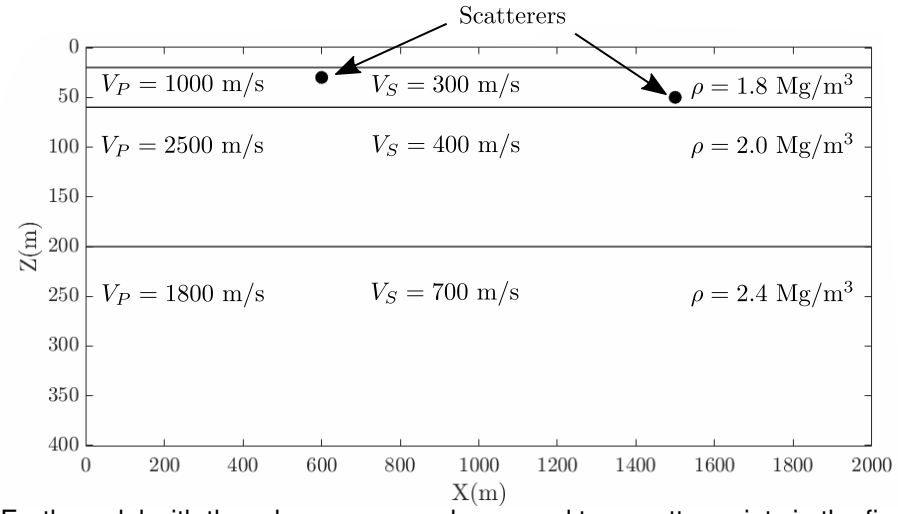

FIG. 2. Earth model with three homogeneous layers and two scatter points in the first layer.

THE PARTITIONED DOMAIN METHOD

Near-surface scattering (NSS) is influenced by not only localized heterogeneities and an irregular bedrock but also by surface topographic variations. In such cases, using the perturbation method with FDM may not be appropriate. We therefore introduce the Partitioned Domain Method (PDM), which is capable of handling complex land areas characterized by rough topography and near-surface parameter variations.

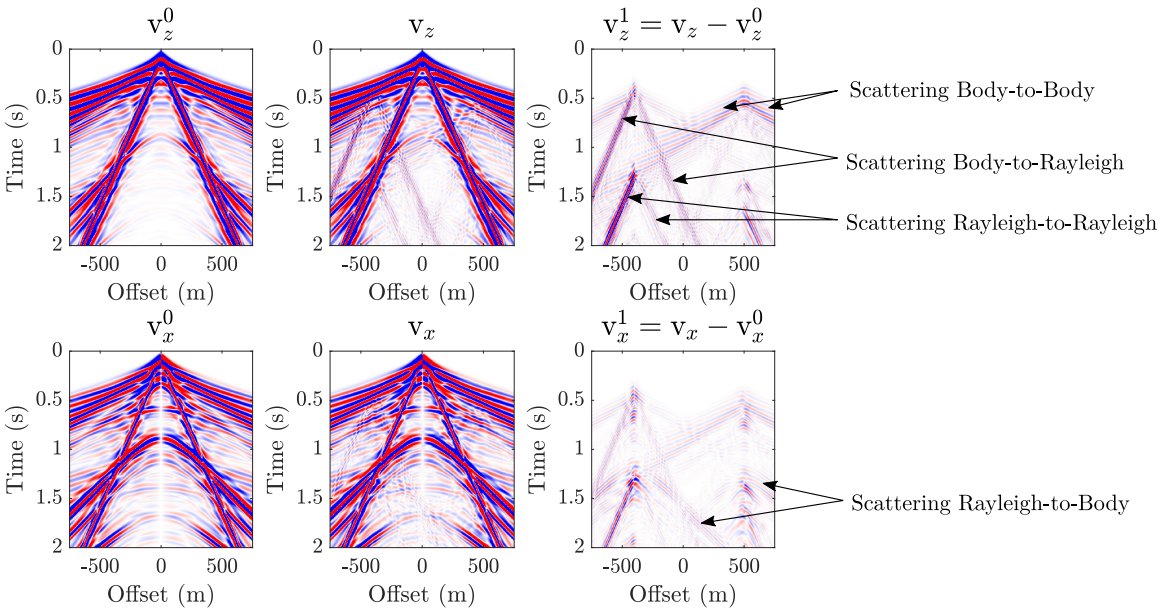

FIG. 3. Scattering wavefield computation using the perturbed method (the difference between total and incident wavefields).

Consider a spatial computational domain, Ω, representing the earth model parameters. This domain can be divided into two subdomains, Ω_1 and Ω_1, as illustrated in Figure 4. The subdomain Ω_1, with a depth of Z_{ns}, refers to the near-surface region, while Ω_2, the portion below Ω_1, denotes deeper structures.

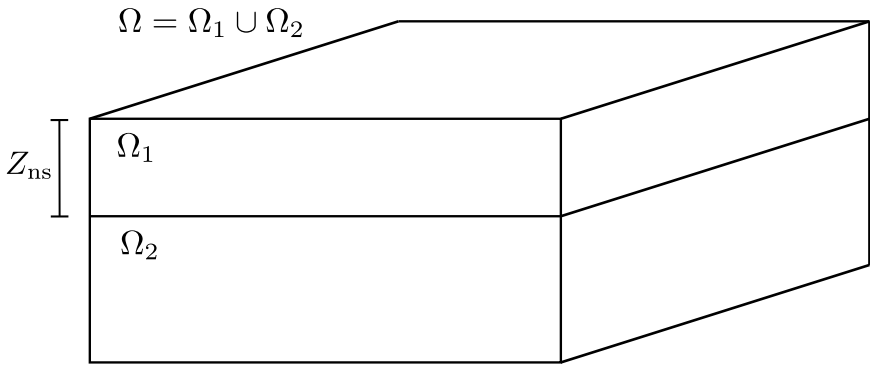

FIG. 4. Partition of the whole domain Ω for the earth model parameters into the subdomains Ω_1 (near-sruface portion) and Ω_2 (deep structures portion). The depth of Ω_1 is represented by Z_{ns}

In the field of exploration seismology, the source is often situated in the near-surface region. This source generates seismic waves, incident body-waves $\mathbf{u}_{\Omega_1}^{0,B}$ and incident Rayleigh waves $\mathbf{u}^{0,R}$, which propagate through the near-surface (Ω_1) (Figure 5(a)). Owing to the presence of heterogeneities with fractional fluctuations of medium parameters ($\delta\mathbf{m}$) in the near-surface region, these incident waves scatter, producing body-wave scattering $\mathbf{u}_{\Omega_1}^{n,B}$ and Rayleigh wave scattering $\mathbf{u}^{n,R}$ (Figure 5(b)).

A portion of the body-wave energy, whether incident or scattering, is transmitted to the deeper structures (Ω_2). Due to the contrast layers, this transmitted energy is reflected back to the near-surface as $\mathbf{u}_{\Omega_2}^{0,B}$ (Figure 5(c)). Upon hitting the near-surface heterogeneities, this

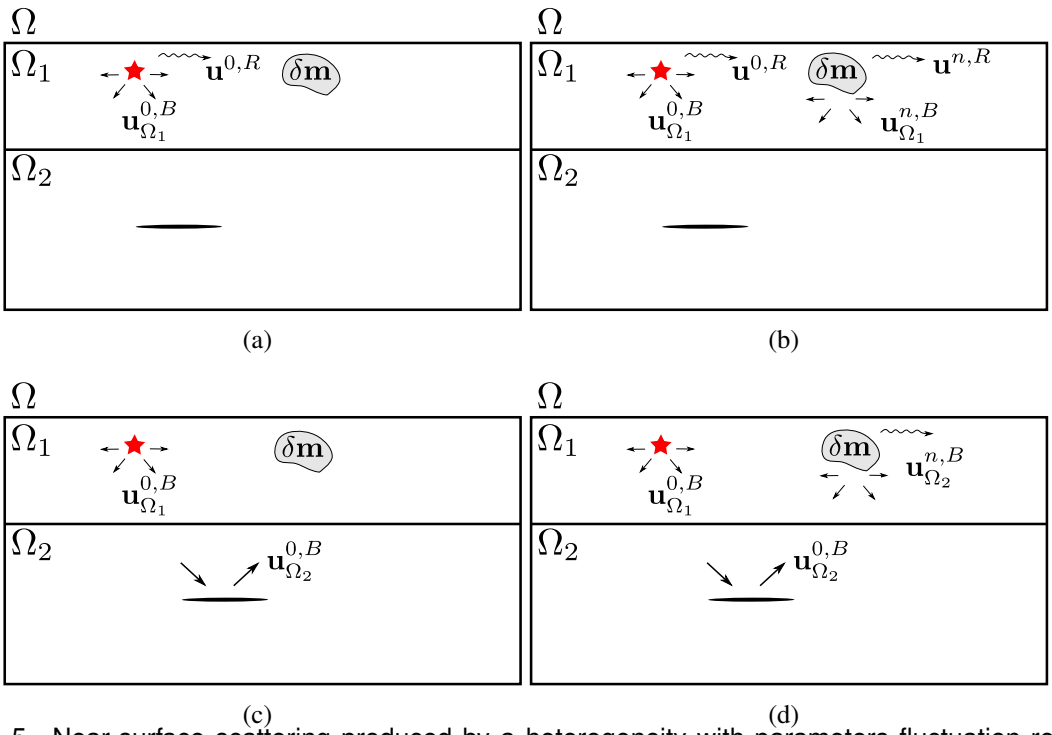

FIG. 5. Near-surface scattering produced by a heterogeneity with parameters fluctuation represented by $\delta\mathbf{m}$. (a) Incident wavefields located in the near-surface segment. (b) Near-Surface Scattering (NSS) of Ω_1 waves. (c) Incident upgoing waves stemming from Ω_2, including reflections and refractions. (d) NSS of upgoing waves originating from Ω_2. The red star denotes the source location. Straight arrows signify the propagation of body waves, while wiggly arrows indicate Rayleigh wave propagation.

reflected energy generates a new scattered wavefield, $\mathbf{u}^{n,B}_{\Omega_2}$ (Figure 5(d)).

Consequently, the total wavefield can be expressed as a superposition of an incident wavefield and NSS as follows:

$$\mathbf{u}_{\mathrm{FW}} = \mathbf{u}^{0,B}_{\Omega_1} + \mathbf{u}^{0,B}_{\Omega_2} + \mathbf{u}^{0,R} + \underbrace{\int \mathbf{G}[-\mathbf{L}(\delta\mathbf{m})] \left(\sum_{n=0}^{\infty} \left(\mathbf{u}^{n,B}_{\Omega_1} + \mathbf{u}^{n,B}_{\Omega_2} + \mathbf{u}^{n,R} \right) \right)}_{\text{NSS: near-surface scattering}}. \tag{24}$$

The NSS can be further decomposed into NSS produced by Ω_1 waves and NSS generated by Ω_2 waves as:

$$\mathbf{u}_{\mathrm{FW}} = \mathbf{u}_{\Omega_1}^{0,B} + \mathbf{u}_{\Omega_2}^{0,B} + \mathbf{u}^{0,R} + \underbrace{\int \mathbf{G}[-\mathbf{L}(\delta\mathbf{m})] \left(\sum_{n=0}^{\infty} \left(\mathbf{u}_{\Omega_1}^{n,B} + \mathbf{u}^{n,R} \right) \right)}_{\text{NSS from } \Omega_1 \text{ waves}} + \underbrace{\int \mathbf{G}[-\mathbf{L}(\delta\mathbf{m})] \left(\sum_{n=0}^{\infty} \left(\mathbf{u}_{\Omega_2}^{n,B} \right) \right)}_{\text{NSS from } \Omega_2 \text{ waves}} \tag{25}$$

During seismic processing in exploration, the filtering stage aims to cleanse the total wavefield and isolate the reflected wavefield, $\mathbf{u}_{\Omega_2}^{0,B}$, which is then used to image the deeper structures.

Near-surface wavefield

The near-surface wavefield, $\mathbf{u}_{\mathrm{NW}}$, represents the solution of the elastic wave equation when only Ω_1 is considered as the computational domain. Consequently, the near-surface wavefield can be derived by excluding Ω_2 waves from equation (25), as depicted below:

$$\mathbf{u}_{\mathrm{NW}} = \mathbf{u}_{\Omega_1}^{0,B} + \mathbf{u}^{0,R} + \underbrace{\int \mathbf{G}[-\mathbf{L}(\delta\mathbf{m})] \left(\sum_{n=0}^{\infty} \left(\mathbf{u}_{\Omega_1}^{n,B} + \mathbf{u}^{n,R} \right) \right)}_{\text{NSS from } \Omega_1 \text{ waves}} \tag{26}$$

In this equation, only the near-surface scattering (NSS) arising from Ω_1 waves are taken into account.

Deep wavefield

The primary objective of PDM method is to obtain a synthetic wavefield that is devoid of NSS. Hence, we define the deep wavefield as the difference between the total wavefield and the near-surface wavefield, as shown below:

$$\mathbf{u}_{\mathrm{DW}} = \mathbf{u} - \mathbf{u}_{\mathrm{NW}} \tag{27}$$

By integrating equations (25) and (26) into (27), we can then express the deep wavefield as:

$$\mathbf{u}_{\mathrm{DW}} = \mathbf{u}_{\Omega_2}^{0,B} + \underbrace{\int \mathbf{G}[-\mathbf{L}(\delta\mathbf{m})] \left(\sum_{n=0}^{\infty} \mathbf{u}_{\Omega_2}^{n,B} \right)}_{\text{NSS from } \Omega_2 \text{ waves}} \tag{28}$$

Please note that while the deep wavefield recovers the energy of the reflected waves, $\mathbf{u}_{\Omega_2}^{0,B}$, it still contains residual energy from the NSS of Ω_2 waves. This implies that the PDM method can be utilized to separate, via simulation, the total wavefield from the NSS of Ω_1 waves. It's important to recognize that the residual NSS from Ω_2 waves is considerably less energetic than the NSS from Ω_1 waves.

Implementation of PDM method

The PDM method can be implemented by following these four steps:

1) Partition the entire domain Ω into two subdomains, Ω_1 and Ω_2, as depicted in Figure (4). The depth of Ω_1, denoted by Z_{ns}, must be manually determined based on the chosen limit for the near-surface portion.

2) Compute the total wavefield $\mathbf{u}$ by numerically solving the elastic wave equation for heterogeneous media (1). This total wavefield comprises both the near-surface wavefield $\mathbf{u}_{\text{NW}}$ and the deep wavefield $\mathbf{u}_{\text{DW}}$ (thus, $\mathbf{u} = \mathbf{u}_{\text{NW}} + \mathbf{u}_{\text{DW}}$).

3) Calculate the near-surface wavefield $\mathbf{u}_{\text{NW}}$ by numerically solving the elastic wave equation for heterogeneous media (1), this time only considering the subdomain Ω_1.

4) Determine the deep wavefield $\mathbf{u}_{\text{DW}}$ by subtracting the near-surface wavefield from the total wavefield (i.e., $\mathbf{u}_{\text{DW}} = \mathbf{u} - \mathbf{u}_{\text{NW}}$).

In the following section, we will present an example of the application of the PDM method, underscoring the advantages of employing this method.

NUMERICAL EXAMPLE WITH THE SEAM FOOTHILLS PHASE II MODEL

To illustrate the effectiveness of the PDM method in modeling NSS, we conducted an experiment using a portion of the SEAM Foothills Phase II model. For the acquisition setup, receivers were arranged on the surface along a line stretching from 500 to 5500 m along the x-axis, with an inter-receiver distance of 10 m, and an explosive source was placed at $\text{X} = 1000$ m. The topographic elevation map for this model, along with the acquisition geometry, is depicted in Figure 6.

In this example, we followed to the steps detailed in subsection , considering three different near-surface depth values, Z_{ns}. Specifically, we set $Z_{\text{ns}} = 1100$, 1300, and 1500 (m). Figure 7 illustrates the boundaries of the near-surface according to these three different depths, within the 2D section of the model in the same plane as the line of receivers.

We utilized the PMFD3D-GPU to solve the elastic wave equation for both the whole domain Ω and the subdomain Ω_1. Snapshots of the propagation for the total, near-surface, and deep wavefields are illustrated in Figure 8. These snapshots correspond to $Z_{\text{ns}} =$1500 (m). It is important to observe that in the near-surface wavefield, seismic energy does not appear for depths below 1500 (m). Additionally, in the deep wavefield, there is noticeable

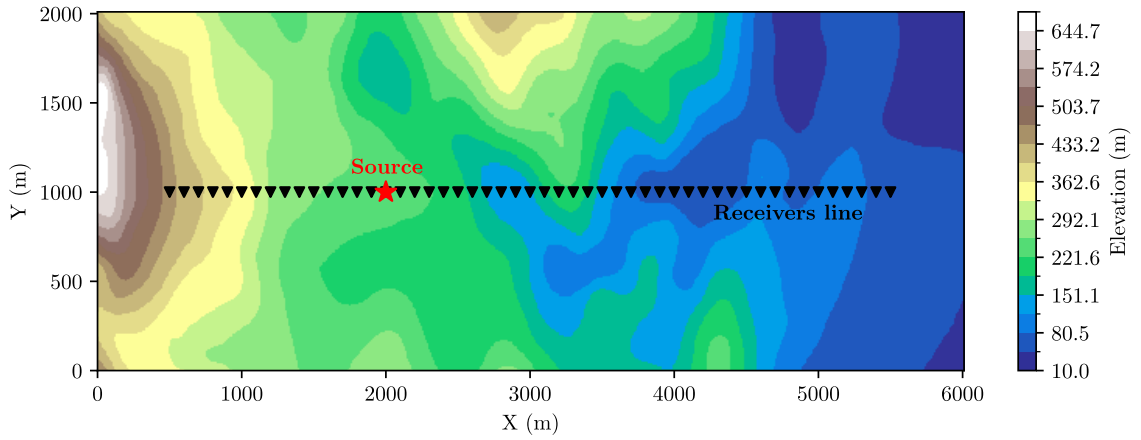

FIG. 6. Elevation map and acquisition geometry for the portion of the SEAM model. The source is positioned at coordinates (200,1000) m, with a depth of 12 m. 3C receivers are aligned on the surface line from 500 to 5500 m at Y=1000 m, with an inter-receiver spacing of 10 m.

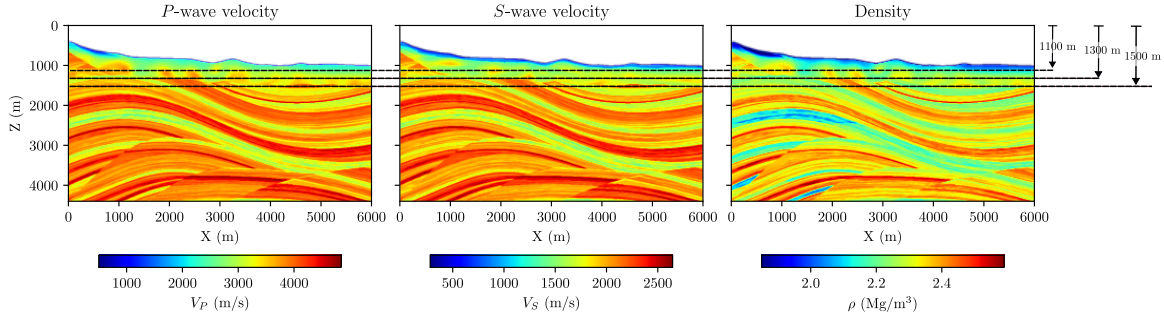

FIG. 7. 2D section of the SEAM portion model sliced along the line of receivers. The topographic elevation map and the acquisition geometry are depicted in Figure 6.

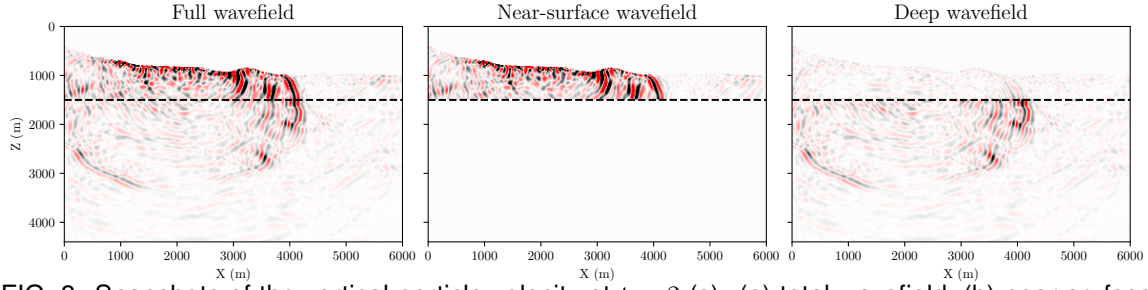

FIG. 8. Snapshots of the vertical particle velocity at $t = 2$ (s). (a) total wavefield, (b) near-sruface wavefield, and (c) Deep wavefield (the difference between (a) and (b)).

energy above the near-surface limit. This corresponds to the upgoing waves from Ω_2 that are not being simulated in the near-surface wavefield.

The multicomponent shot gather for the total wavefield exhibits various wave types such as Rayleigh waves, refractions, reflections, and NSS (as illustrated in Figure 9). Similarly, the multicomponent shot gathers for the near-surface wavefields also exhibit various wave types. However, these wavefields do not contain waves from the Ω_2 subdomain, as indicated in equation 26. It is observed that the deeper the near-surface portion, the more pronounced the energy of refraction events becomes. In the multicomponent shot gathers of the deep wavefield, which were obtained by subtraction, it is evident that more refraction energy is present when the near-surface portion is more shallow.

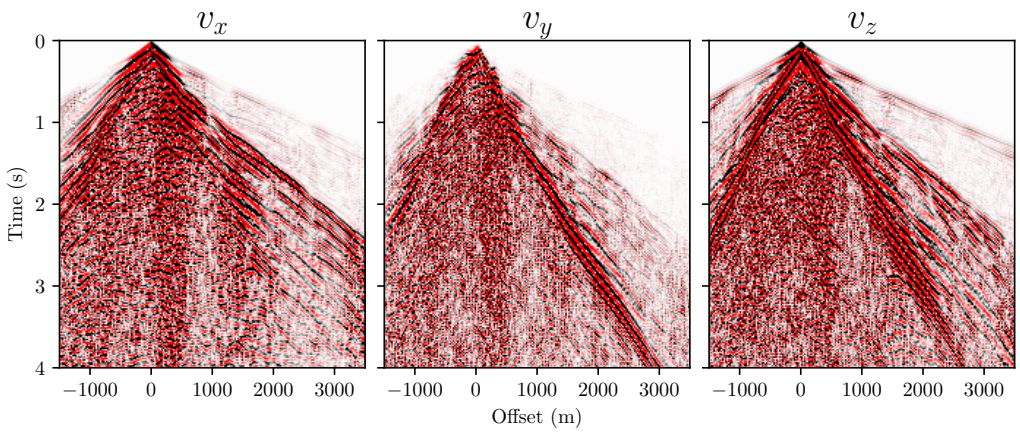

FIG. 9. Multicomponet shot gather for the total wavefield acquired in the portion of the SEAM Foothills model using whole domain.

We conducted an analysis to quantify the energy proportion of the near-surface wavefield and the deep wavefield in relation to the total wavefield. The results, presented in Table 1, demonstrate that the total wavefield is predominantly composed of the near-surface wavefield, with only a minor portion of the energy attributed to the deep wavefield. Specifically, in the x- and z-components, the near-surface wavefield accounted for over 99.7% of the total energy across all three different depths of the near-surface portion. Consequently, the deep wavefields represented 0.3% or less of the total energy.

Ω_1 depth (m)	Near-surface wavefield			Deep wavefield		
	v_x (%)	v_y (%)	v_z (%)	v_x (%)	v_y (%)	v_z (%)
1100	99.72	97.17	99.74	0.28	2.83	0.26
1300	99.79	97.93	99.80	0.21	2.07	0.20
1500	99.97	99.61	99.97	0.03	0.39	0.03

Table 1. Percentage of composition of near-surface wavefield and deep wavefield in relation to the total wavefield

DISCUSSION

The proposed PDM has demonstrated its efficacy as a strategy for modeling NSS in complex overburden scenarios, which include rough topography and random media. This is a distinct advantage over existing methods, such as the analytical perturbation method, asymptotic methods, integral equation, and FDM with perturbation method. These conventional methods typically assume constant background medium parameters and rely on the homogeneous wave equation to simulate the incident wavefield. Contrary to these methods, our PDM does not make this assumption, thereby enabling the generation of incident waves in heterogeneous background models. This capability leads to a more accurate modeling of NSS in complex environments.

Our mathematical model revealed that partitioning the computational domain makes it possible to separate the total wavefield into two components: the near-surface wavefield and the deep wavefield. Numerical results obtained with the SEAM foothills model confirmed that a significant majority of seismic energy (around 99%) was localized in the near-surface wavefield, while only a minor fraction (about 1%) was detected in the deep wavefield (see

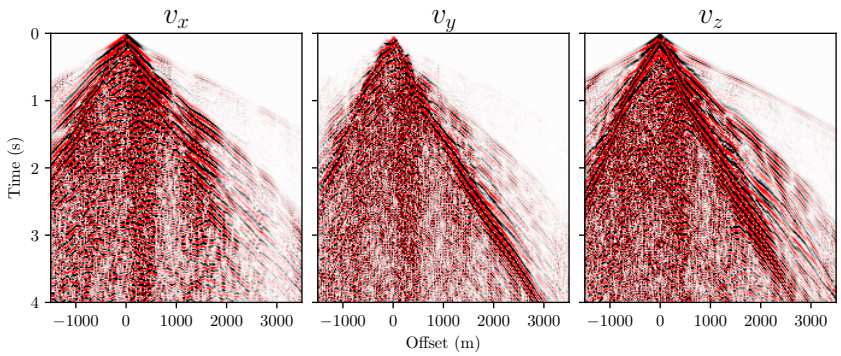

(a)

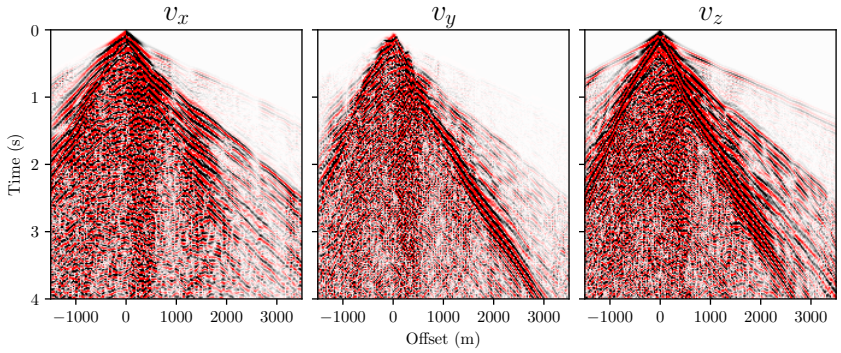

(b)

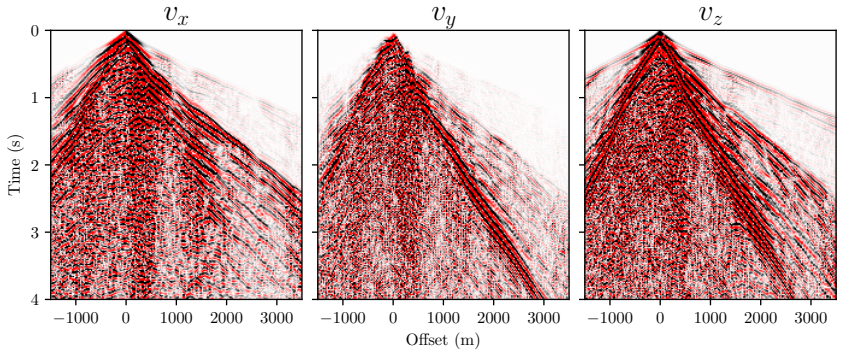

(c)

FIG. 10. Multicomponent shot gather of the near-surface wavefield with different depths of near-surface subdomain. (a) Z_{ns} =1100 (m). (b) Z_{ns} =1300 (m). (c) Z_{ns} =1500 (m).

Table 1). Despite their lower energy, deep wavefields carry all the energy of the upcoming waves, which are essential for imaging deeper geological structures.

The principal contribution of the PDM is its ability to generate ideal synthetic data devoid of ground roll. Our numerical examples clearly showed that the resulting deep wavefields are free from wave types often classified as coherent noise, including Rayleigh waves, near-surface refractions, reflections, and most near-surface scattering (see Figure 11). The simulated deep wavefield can thus serve as a synthetic gold standard, facilitating the validation and comparison of new filtering techniques. Furthermore, the generation of

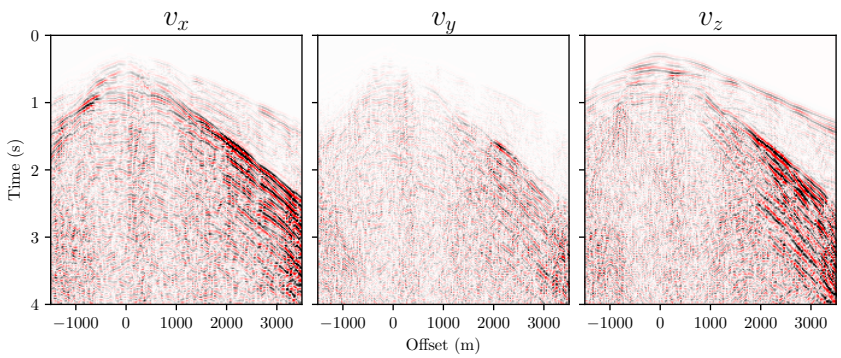

(a)

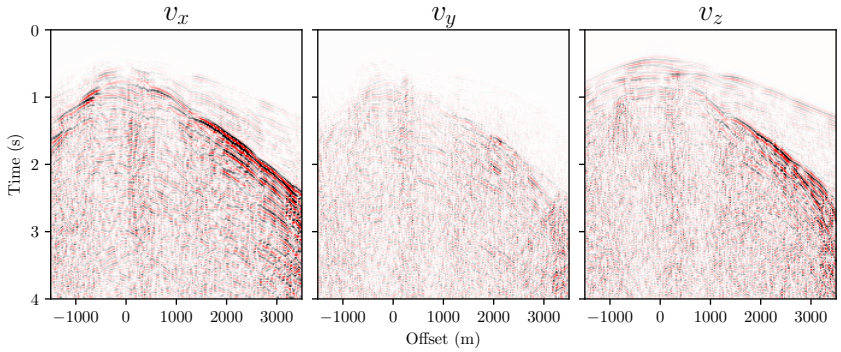

(b)

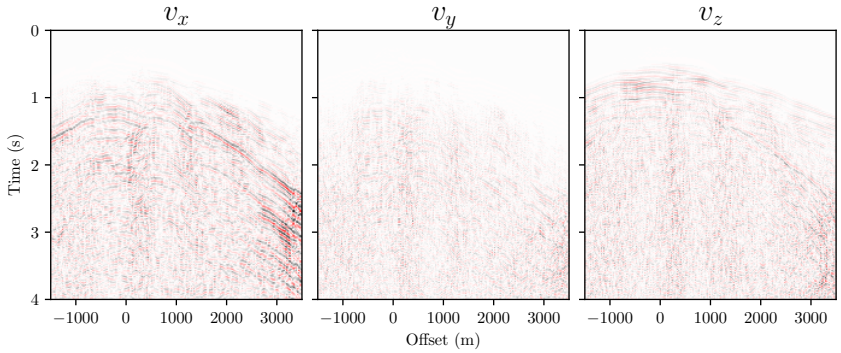

(c)

FIG. 11. Multicomponent shot gather of the deep wavefield with different depths of near-surface subdomain. (a) Z_{ns} =1100 (m). (b) Z_{ns} =1300 (m). (c) Z_{ns} =1500 (m).

these synthetic gold standards proves advantageous for training machine learning models, as producing thousands of synthetic datasets is significantly more cost-effective and less time-consuming than collecting real seismic data. All these aspects underscore the utility of the PDM for the advancement of seismic processing techniques.

While the PDM clearly offers numerous benefits, it's crucial to also consider its limitations. One significant limitation stems from the formulation of the method itself. The PDM is designed to separate NSS by treating it as an additive process rather than a multiplicative one. This approach results in an incomplete isolation of NSS from the total wavefield, as

demonstrated by equation (27), which indicates that the deep wavefield still retains some NSS produced by the upcoming waves. However, the residual NSS is considerably less energetic than that found in the near-surface wavefield (Figures 10 and 11), allowing the PDM to remain a viable tool for simulating synthetic data free from ground roll. Another limitation involves setting the domain partition through the adjustment of the Z_{ns} value. This value must be manually calibrated based on the near-surface depth. Our numerical example shows that larger Z_{ns} values yield a near-surface wavefield with higher energy, and correspondingly, a deep wavefield with lower energy (see Table 1). Thus, users must experiment with various Z_{ns} values to obtain the desired wavefield results from the PDM.

CONCLUSIONS

In this work, we have presented the Partitioned Domain Method (PDM) as an innovative approach to model NSS in complex overburden scenarios characterized by rough topography and random media. By employing a domain partitioning technique, the PDM separates the total wavefield into distinct near-surface and deep wavefields, enabling more accurate simulations. Notably, the PDM stands out from existing methodologies by eliminating the assumption of constant background medium parameters and facilitating the generation of incident waves in heterogeneous background models. Although the PDM exhibits limitations, such as the incomplete isolation of NSS and the requirement for manual calibration of the domain partition, the resulting synthetic wavefields offer valuable synthetic data devoid of ground roll. These synthetic datasets serve as a gold standard for the validation and comparison of novel filtering techniques. Furthermore, the generation of synthetic data holds significant potential for advancing seismic processing techniques and training machine learning models aimed at attenuating scattering noise. Future research efforts should focus on addressing the limitations of the PDM, enhancing its performance, and expanding its applicability in the field of near-surface scattering modeling.

REFERENCES

Almuhaidib, A. M., and Toksöz, M. N., 2014, Numerical modeling of elastic-wave scattering by near-surface heterogeneities: Geophysics, **79**, No. 4, T199–T217.

Beylkin, G., and Burridge, R., 1990, Linearized inverse scattering problems in acoustics and elasticity: Wave motion, **12**, No. 1, 15–52.

Blonk, B., and Herman, G. C., 1994, Inverse scattering of surface waves; a new look at surface consistency: Geophysics, **59**, No. 6, 963–972.

Campman, X., and Dwi Riyanti, C., 2007, Non-linear inversion of scattered seismic surface waves: Geophysical Journal International, **171**, No. 3, 1118–1125.

Hudson, J., 1967, Scattered surface waves from a surface obstacle: Geophysical Journal International, **13**, No. 4, 441–458.

Maeda, T., Sato, H., and Nishimura, T., 2008, Synthesis of coda wave envelopes in randomly inhomogeneous elastic media in a half-space: single scattering model including rayleigh waves: Geophysical Journal International, **172**, No. 1, 130–154.

Riyanti, C. D., and Herman, G. C., 2005, Three-dimensional elastic scattering by near-surface heterogeneities: Geophysical Journal International, **160**, No. 2, 609–620.

Robertsson, J. O., and Chapman, C. H., 2000, An efficient method for calculating finite-difference seismograms after model alterations: Geophysics, **65**, No. 3, 907–918.

Sato, H., Fehler, M. C., and Maeda, T., 2012, Seismic wave propagation and scattering in the heterogeneous earth: Springer Science and Business Media.

Snieder, R., 1986, 3-d linearized scattering of surface waves and a formalism for surface wave holography: Geophysical Journal International, **84**, No. 3, 581–605.

Wu, R.-S., 1989, The perturbation method in elastic wave scattering, *in* Scattering and Attenuation of Seismic Waves, Part II, Springer, 605–637.

Wu, R.-S., and Aki, K., 1985, Scattering characteristics of elastic waves by an elastic heterogeneity: Geophysics, **50**, No. 4, 582–595.

Yilmaz, Ö., 2015, Engineering seismology with applications to geotechnical engineering: Society of Exploration Geophysicists.